Video Article

Proof-of-Concept for Gas-Entrapping Membranes Derived from Water-Loving SiO_2/Si/SiO_2 Wafers for Green Desalination

Ratul Das[1], Sankara Arunachalam[1], Zain Ahmad[1], Edelberto Manalastas[1], Ahad Syed[2], Ulrich Buttner[2], Himanshu Mishra[1]

[1]Water Desalination and Reuse Center (WDRC), Biological and Environmental Science and Engineering (BESE) Division, King Abdullah University of Science and Technology (KAUST)

[2]Core Labs, King Abdullah University of Science and Technology (KAUST)

Correspondence to: Himanshu Mishra at himanshu.mishra@kaust.edu.sa

URL: https://www.jove.com/video/60583
DOI: doi:10.3791/60583

Keywords: water desalination, direct contact membrane distillation, perfluorocarbon-free membranes, photolithography, reactive-ion etching, wetting, reentrant features, chrome masking, back alignment, anisotropic etching, vapor transport

Date Published: 1/12/2020

Citation: Das, R., Arunachalam, S., Ahmad, Z., Manalastas, E., Syed, A., Buttner, U., Mishra, H. Proof-of-Concept for Gas-Entrapping Membranes Derived from Water-Loving SiO_2/Si/SiO_2 Wafers for Green Desalination. *J. Vis. Exp.* (), e60583, doi:10.3791/60583 (2020).

Abstract

Desalination through direct contact membrane distillation (DCMD) exploits water-repellent membranes in order to robustly separate counterflowing streams of hot and salty seawater from cold and pure water, thus allowing only pure water vapor to travel through. To achieve this feat, commercial DCMD membranes are derived from or coated with perfluorocarbons such as polytetrafluoroethylene (PTFE) and polyvinylidene difluoride (PVDF). However, use of perfluorocarbons is limited due to their high cost, non-biodegradability, and vulnerability to harsh operational conditions. Unveiled here is a new class of membranes referred to as gas-entrapping membranes (GEMs) that can robustly entrap air upon immersion in water. This property is due to their surface architecture rather than surface chemistry. This work demonstrates a proof-of-concept for GEMs using intrinsically wetting silicon wafers with a thermally grown oxide layer (SiO_2) as the model system. The contact angle of water on SiO_2 is $\theta_0 \approx 40°$. GEMs are comprised of arrays of pores whose diameters increase abruptly (i.e., with a 90° turn) at the inlets and outlets, also known as the "reentrant" edges. Methods for the microfabrication of silica-GEMs that include designing, photolithography, chrome sputtering, and isotropic and anisotropic etching are presented below. The efficacy of GEMs is underscored by the fact that silica membranes with simple cylindrical pores spontaneously imbibe water (<1 s), whereas air entrapped in silica-GEMs underwater remains intact even after 6 weeks (>10^6 s). While the choice of SiO_2/Si wafers for GEMs is limited to demonstrating the proof-of-concept, it is believed that the concepts presented here will advance the rational design of scalable GEMs using inexpensive wetting materials for desalination and beyond.

Video Link

The video component of this article can be found at https://www.jove.com/video/60583/

Introduction

As the stress on water/food/energy/environmental resources increases, greener technologies and materials for desalination (i.e., harnessing renewable energy and common inexpensive materials) are needed[1,2]. In this context, the DCMD process can utilize solar-thermal energy or waste industrial heat for water desalination[3,4]. DCMD exploits water-repellent membranes to separate counterflowing streams of hot seawater and cold deionized water, allowing only pure water vapor to travel from the hot to cold side[5,6,7,8,9].

Commercial DCMD membranes almost exclusively exploit perfluorocarbons because of their water repellency, characterized by the intrinsic contact angle of water on perfluorocarbons ($\theta_0 \approx 110°$)[10]. However, perfluorocarbons are expensive, and they become damaged at elevated temperatures[11] and upon harsh chemical cleaning and abrasion[12,13]. Their non-biodegradability also raises environmental concerns[14]. Thus, new materials for DCMD have been explored (i.e., polypropylene[15], carbon nanotubes[16], and organosilica[17]), along with variations of the process (i.e., interfacial heating[18] and photovoltaic-MD[19]). Nevertheless, all materials investigated for the use of DCMD thus far have been intrinsically water-repellent (i.e., characterized by $\theta_0 \geq 90°$ for water).

Here, a protocol is described for exploiting water-loving (hydrophilic) materials for the use of water-repellent DCMD membranes (i.e., separating water on either side by entrapping air robustly inside the membrane pores). Through a proof-of-concept demonstration, double-sided polished silicon wafers with silica layers (2 µm thick) on both sides (SiO_2/Si/SiO_2; 2 µm/300 µm/2 µm, respectively) are used. Microfabrication processes are applied to achieve gas entrapping membranes (GEMs), which exploit a specific architecture to prevent liquids from entering the pores regardless of surface chemistry.

The inspiration for GEM architecture originated from springtails (Collembola class of animals), soil-dwelling hexapods whose cuticles contain mushroom-shaped patterns[20,21], as well as sea-skaters (*Halobates germanus*), insects living in the ocean that have mushroom-shaped hair on their legs[22,23]. The surface architecture, along with naturally secreted waxes, affords these insects with "super" water repellence, characterized by apparent contact angles for water ($\theta r \geq 150°$:)[24]. As a result, when these insects contact water, air becomes trapped inside the hairs on their

legs, which reduces hydrodynamic drag[22,25]. If submerged in water, these insects instantaneously trap a layer of air (also known as plastron) in the microtexture surrounding the body, which facilitates respiration and buoyancy[20,23].

Inspired by springtails, Kim and colleagues showed that silica surfaces with arrays of mushroom-shaped pillars can repel droplets of liquids with low surface tension[26]. This was a remarkable discovery; albeit, it was found that the liquid repellence of these surfaces could be lost catastrophically through localized defects or boundaries[27,28]. To remedy this problem, researchers microfabricated silica surfaces with cavities whose diameters at the inlets were abruptly smaller (i.e., with a 90° turn) than the rest of the cavity[27]. These features are also known as "reentrant" edges, and the cavities are hereafter referred to as "reentrant cavities".

Silica surfaces with reentrant cavities exhibit robust repellency to liquids due to the robust entrapment of air inside when contacting drops or upon submersion in liquid[27]. The performance of cavities of different shapes (circular, square, and hexagonal), profiles (reentrant and doubly reentrant), and sharpness of corners in relation to the stability of entrapped air inside over time has been compared[29]. It has been found that circular reentrant cavities are the most optimal in terms of their robustness for air entrapment underwater and the complexity associated with manufacturing. Also, it has been demonstrated that hydrophilic surfaces with reentrant cavities can function hydrophobically by entrapping air upon immersion in water. Additionally, this feature may not be captured by only measuring receding contact angles[28]. Based on this body of work[27,28,29,30] and previous experience with DCMD[31], we decided to create membranes that have pores with reentrant inlets and outlets. It was envisioned that such a membrane will entrap air upon immersion in wetting liquids, giving rise to the idea of GEMs.

Consider a membrane made from a hydrophilic material comprising simple cylindrical pores: when immersed in water, this membrane will imbibe water spontaneously (**Figure 1A,B**) in accordance with Wenzel's model[32]. On the other hand, if the inlets and outlets of the pores have reentrant profiles (e.g., are "T"-shaped), they may prevent the wetting liquid from penetrating the pore and entrap air inside, leading to the Cassie state[33] (**Figure 1C,D**). Once the air is trapped inside the pore, it will further prevent liquid intrusion due to its compressibility and low solubility in water over time[34,35].

Such a system will slowly transition from Cassie to Wenzel states, and the kinetics of this process can be tuned by the cavity's shape, size, and profile; vapor pressure of the liquid; and solubility of the trapped air in the liquid[29,34,36]. Researchers have been able to realize GEMs using silicon wafers and polymethylmethacrylate sheets as the test substrates, and proof-of-concept applications for DCMD in a cross-flow configuration have been demonstrated[37]. Here, a detailed microfabrication protocol for the generation of silica-GEMs, starting with double-sided polished silicon wafers (300 µm thick), is presented. Also, the ability of the silica-GEMs to entrap air underwater using a custom-built pressure cell and confocal microscopy is unveiled.

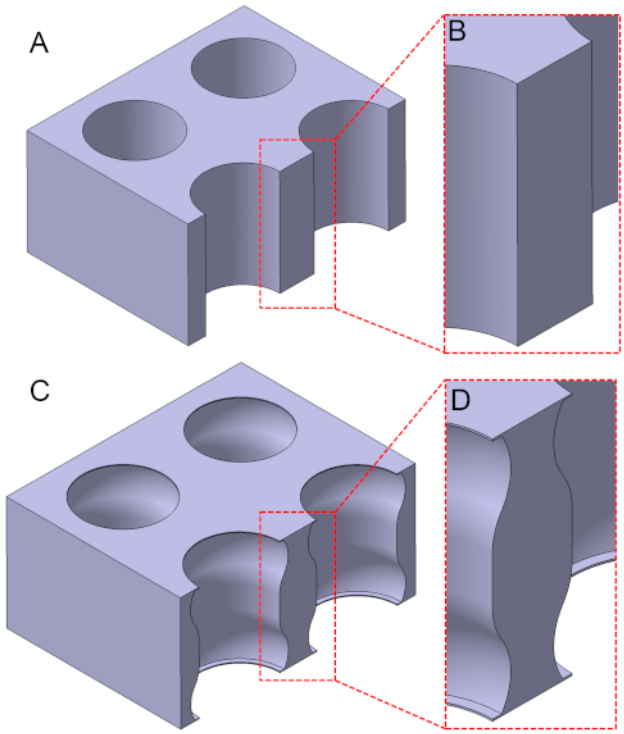

Figure 1: **Schematic representation of a membrane with simple cylindrical pores (A,B) and one with reentrant pores (C,D).** In contrast to the simple cylindrical pores, the reentrant pores become sharply broader after inlets/outlets, and it is this discontinuity (or the reentrant edges) that prevents liquids from intruding into the pores. Please click here to view a larger version of this figure.

In particular, this protocol describes a microfabrication protocol for carving arrays of pores reentrant inlets and outlets using double-sided polished silicon wafers that are 300 µm thick (p-doped, <100> orientation, 4" diameter, 2 µm thick thermally grown oxide layers on both sides). This is referred to hereafter as SiO_2(2 µm)/Si(300 µm)/SiO_2(2 µm) (**Figure 2**).

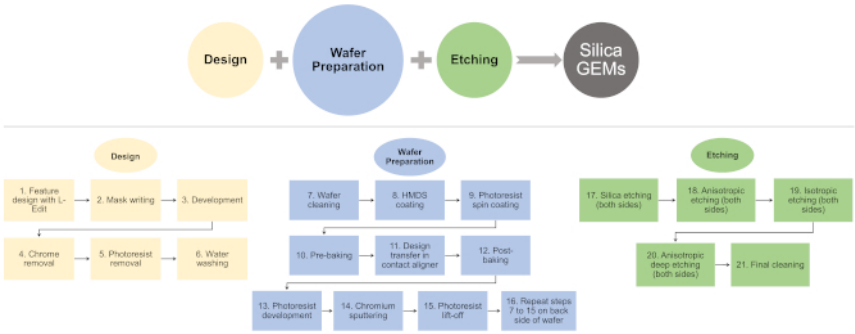

Figure 2: Flowchart listing key steps involved in the microfabrication of silica-GEMs. Please click here to view a larger version of this figure.

Protocol

1. Design

1. Design 16 arrays, each comprising 625 circles (diameter, D = 100 µm; pitch, L = 400 µm), along with alignment marks to be translated onto 4" SiO_2(2 µm)/Si(300 µm)/SiO_2(2 µm) wafers using appropriate design software (see **Table of Materials**; **Figure 3**)[38].

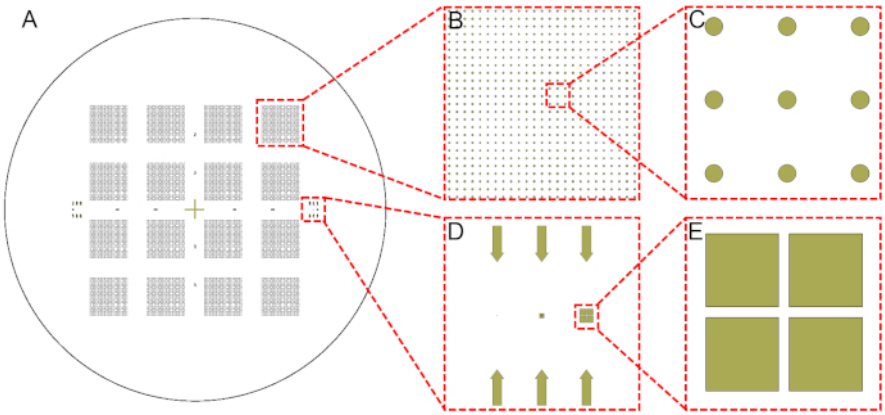

Figure 3: Designs of circular arrays. This design pattern was transferred onto SiO_2(2 µm)/Si(300 µm)/SiO_2(2 µm) wafers through photolithography. Shown are (**A**) the entire wafer, (**B**,**C**) zoomed-in views, and (**D**,**E**) alignment marks used for the manual back alignment. Please click here to view a larger version of this figure.

2. Transfer features onto a 5" soda lime glass ($Ca_xH_yNa_zO_n$) mask with a 50 nm coating of chromium and thin film of photoresist (a positive photoresist; see **Table of Materials**) through UV exposure in a direct-writing system (exposure time = 25 ms, defocus = +10).
3. Mask development
    1. Develop the photoresist by immersing the mask in 200 mL of developer (**Table of Materials**) for 60 s to expose the chrome underneath. Wash the mask with deionized (DI) water.
    2. Remove the exposed chromium by immersing the mask in a 200 mL bath of chrome etchant for 90 s. Wash the mask with DI water.
    3. Carry out a UV flood exposure (i.e., without mask) for 15 s.
    4. Completely remove photoresist from the mask by immersing in a 200 mL bath of developer until the photoresist completely disappears (60–120 s). Clean the mask surface with DI water and dry using a nitrogen (N_2) gun.

2. Wafer cleaning

1. Immerse the silicon wafer in a freshly prepared piranha solution (H_2SO_4:H_2O_2 = 3:1 by volume) maintained at a temperature of 388 K for 10 min.
   NOTE: Wear appropriate personalized protection equipment (PPE) while working with piranha solution on the wet bench.
2. Rinse the wafer with DI water, two cycles in a wet bench, and dry it under a N_2 environment in spin drier.

3. HMDS deposition

1. Expose the wafer to the vapor of hexamethyldisilane (HMDS) to improve adhesion of the photoresist with the silica surface (details in **Table 1**).

Stage 1: Dehydration and purging oxygen from chamber		
Step	**Function**	**Time (min)**
1	Vacuum (10 Torr)	1
2	Nitrogen (760 Torr)	3
3	Vacuum (10 Torr)	1
4	Nitrogen (760 Torr)	3
5	Vacuum (10 Torr)	1
6	Nitrogen (760 Torr)	3
Stage 2: Priming		
Step	**Function**	**Time (min)**
1	Vacuum (1 Torr)	2
2	HMDS (6 Torr)	5
Stage 3: Purging Prime Exhaust and Return to Atmosphere (Backfill)		
Step	**Function**	**Time (min)**
1	Vacuum	1
2	Nitrogen	2
3	Vacuum	2
4	Nitrogen	3

Table 1: HMDS priming process details.

4. Lithography

1. Transfer the wafer onto a vacuum-chuck of a spin coater to spin coat the photoresist. Use AZ 5214 photoresist as a negative tone to achieve a 1.6 µm thick uniform film of the photoresist (the spin coating parameters are listed in **Table 2**).
   NOTE: AZ 5214 can be used as a positive or negative tone photoresist based on the heat treatment (i.e., pre-baking and post-baking). If prebaked at 110 °C for 2 min, the photoresist behaves as a positive tone, such that exposed areas become dissolved during development. For the negative tone, the photoresist is prebaked at 105 ° C for 2 min followed by UV exposure and post-baking at 120 °C for 2 min.
   1. Bake the photoresist-coated wafer at 105 °C on a hotplate for 2 min. This dries and hardens the photoresist film, which otherwise sticks to the glass mask and causes contamination issues during UV exposure, and it also improves adhesion of the photoresist to the silica surface.
      NOTE: The pre-bake temperature should not be too high, as this may cause the partial destruction of light-sensitive components of the photoresist, reducing its sensitivity.

Step	**Speed (rpm)**	**Ramp (rpm/s)**	**Time (s)**
1	800	1000	3
2	1500	1500	3
3	3000	3000	30

Table 2: Parameters for spin coating recipe to obtain a 1.6 µm layer of photoresist.

2. Expose the wafer under UV exposure (80 mJ/cm^2) for 15 s through the chrome mask using a mask alignment system (EVG 6200) to achieve the desired design on the photoresist.
3. Bake the realized wafer at 120 °C on a hotplate for 2 min. During this step, the exposed negative photoresist film further cross-links. As a result, the UV-exposed parts of the photoresist are no longer soluble in the developer solution, while the unexposed areas are soluble.
4. Further expose the wafer under UV light (200 mJ/ cm^2) for 15 s in a UV cure system (PRX-2000-20).
   NOTE: During this step, the photoresist areas that were not previously exposed (step 4.3) are exposed and can later be dissolved in the developer, leaving behind the desired structures on the wafer. This step is tolerant of overexposure because the desired features (in the negative tone) are no longer photosensitive after the post-baking step.
5. Immerse the wafer in a 50 mL bath of the AZ-726 photoresist-developer (in glassware) for 60 s to achieve the desired photoresist pattern on the silicon wafer.
6. Subsequently clean the wafer using DI water and further blow-dry it with N_2.

5. Sputter

1. Sputter chromium on the wafer for 200 s to obtain a 50 nm thick chromium layer. The deposition is performed using a magnetron-type DC reactive sputter with a standard 2” round target source in an argon environment with the following parameters: 400 V, current = 1 A, and pressure = 5 mTorr.
   NOTE: The chrome layer protects silica from dry etching under octafluorocyclobutane (C_4F_8).

6. Photoresist lift-off

1. Sonicate the sputtered wafer in an acetone bath for 5 min to lift off the remaining photoresist (and chromium deposited on the photoresist) from the wafer, leaving behind the desired features with a chromium hard mask.

7. Processing of the other side of the wafer

1. After rinsing the backside of the wafer with a copious amount of acetone and ethanol, blow-dry with an N_2 gun, then repeat steps 4.1 and 4.2.

8. Manual back alignment

1. Align the desired features on the backside with the front side of the wafer using the alignment marks in the design and the “Manual back alignment with crosshair” module in the contact aligner (EVG 6200).
   NOTE: Manual back alignment is a crucial step in the microfabrication protocol. Thus, the designed alignment features on the photomask must be used effectively to avoid offset in pore alignment.

9. Lithography on the backside of the wafer

1. For the backside of the wafer, repeat steps 4.3–4.7, section 5, and section 6 to generate the required design with chromium on both sides of the wafer. Note that the part of surface covered with chromium does not undergo etching; thus, spots in which chromium is absent on the wafer define the inlets and outlets of the pore.

10. Etching

1. Undergo etching of the exposed SiO_2 layer on both sides of the wafer by an inductively coupled plasma (ICP) reactive ion etcher (RIE) that employs fluorine (C_4F_8) and oxygen (O_2) chemistries. The duration is 16 min (ICP-RIE parameters listed in **Table 3**) for each side.
2. Process the wafer with five cycles of anisotropic etching using the Bosch process to create a notch in the silicon layer. This process is characterized by a flat sidewall profile using alternating depositions of C_4F_8 and sulfur hexafluoride (SF_6) gases. By alternating anisotropic etching and polymer deposition, the silicon etches straight down (etching parameters listed in **Table 3**).
3. To create the undercut, which yields the reentrant profile, undergo isotropic etch using an SF_6-based re[illegible]or a duration of 165 s (etching parameters listed in **Table 3**).
   NOTE: This step is performed on each side of the wafer.
4. Anisotropic silicon etching
   1. Transfer the wafer to deep-ICP-RIE (Oxford instruments) to etch 150 µm of silicon using 200 cycles of deep etching using the Bosch process (etching parameters are listed in **Table 3**).
   2. Repeat step 10.4.1 with the backside of the wafer.
   3. Undergo piranha cleaning of the wafer in the wet bench for 10 min to remove polymeric contaminants deposited from the etching process, which ensures uniform etching rates.
   4. Repeat steps 10.4.1–10.4.3 to realize through pores (which can be visualized by naked eyes under a light source) in the wafer having reentrant inlets and outlets.

Parameter	Silica Etching	Anisotropic silicon etching /cycle		Isotropic silicon etching
		Deposition	Etching	
RF power (W)	100	5	30	20
ICP power (W)	1500	1300	1300	1800
Etching pressure (mTorr)	10	30	30	35
Temperature (°C)	10	15	15	15
C_4F_8 flow (sccm)	40	100	5	-
O_2 flow (sccm)	5	-	-	-
SF_6 flow (sccm)	-	5	100	110
Etching time (s)	960	5	7	165

Table 3: Parameters for SiO_2/Si dry etching.

11. Final cleaning

1. After the microfabrication process, clean the wafer with 100 mL of freshly prepared piranha solution (H_2SO_4:H_2O_2 = 3:1 by volume; T = 388 K) in a glass container for 10 min, then further blow-dry with a 99% pure N_2 pressure gun.
2. Place the samples in a glass Petri dish inside a clean vacuum oven at T = 323 K until the intrinsic contact angle of water on smooth SiO_2 is stabilized at $\theta_0 \approx 40°$ (after 48 h).
3. Store the obtained dry samples (silica GEMs) in a N_2 cabinet.
   NOTE: The entire fabrication workflow is depicted in **Figure 4**.

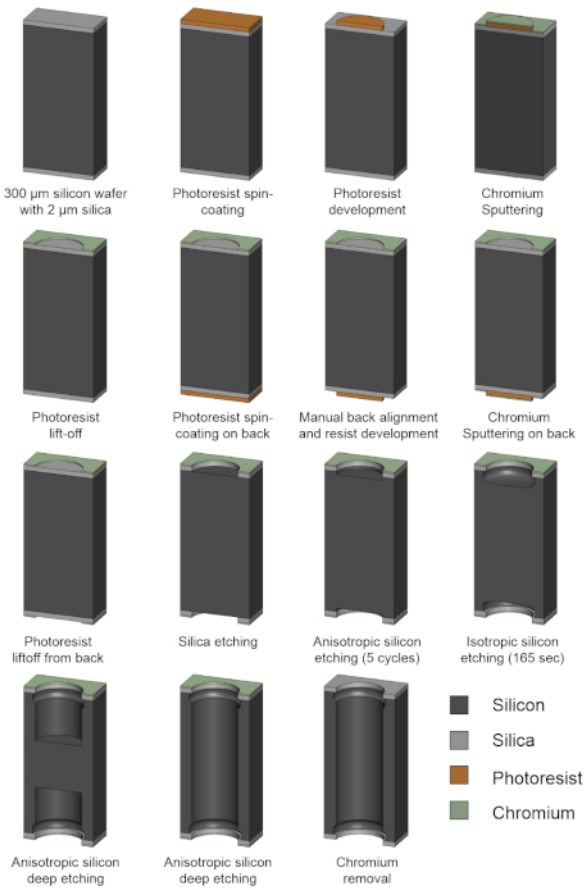

Figure 4: Schematic illustration of the GEM microfabrication process. Please click here to view a larger version of this figure.

Representative Results

This section presents the underwater performance of silica-GEMs microfabricated using the abovementioned protocols. The pores of these GEMs were vertically aligned, inlet/outlet diameters were D = 100 µm, center-to-center distance between the pores (pitch) was L = 400 µm, separation between the reentrant edges and pore wall was w = 18 µm, and length of the pores was h = 300 µm (**Figure 5**). Due to inhomogeneities during etching steps and minor misalignment during microfabrication, the middle portion of the pores could have been a bit narrower compared to the portion below the inlets and outlets of the pores. However, for the results reported here, it did not affect the mass flux significantly.

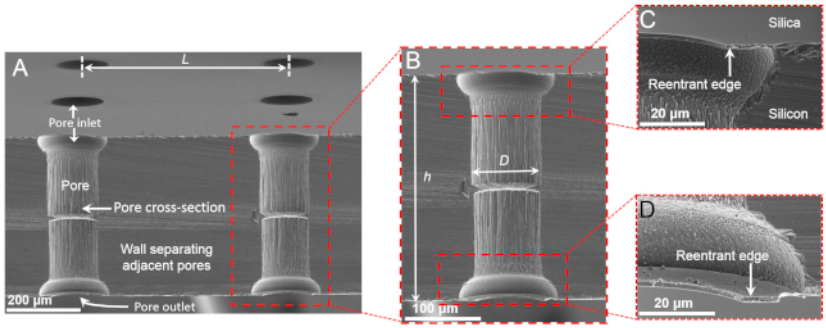

Figure 5: Scanning electron micrographs of silica-GEMs. Shown are (**A**) a tilted cross-sectional view of silica-GEMs, (**B**) a magnified cross-sectional view of a single pore, and (**C,D**) magnified views of reentrant edges at the inlets and outlets of a pore. Panels (C) and (D) are reprinted from Das et al.[37]. Please click here to view a larger version of this figure.

Immersing silica-gems in water

Silica (SiO_2) surfaces are hydrophilic, as characterized by the intrinsic contact angle of water drops on silica under saturated water vapor (θ_0 ≈ 40°). Thus, based on Wenzel's model, it is expected that if a silica surface is rougher (i.e., by creating pores/cavities on it), then the resulting surface will be even more hydrophilic[32].

To test this prediction, a custom-built module was employed that can secure a test-membrane between a reservoir of dyed salty water (~0.6 M NaCl with food coloring) and deionized water (T = 293 K and p = 1 atm). It accomplishes this while simultaneously logging the electrical conductivity of the deionized water reservoir into a computer to monitor pore filling in situ (**Figure 6A**). Here, silica membranes with simple cylindrical holes were not able to prevent the mixing of the two reservoirs, since water infiltrated instantaneously as reflected by the release of dye (**Movie S1**).

In sharp contrast, when silica-GEMs were tested under the same conditions, they robustly entrapped air and held it intact for over 6 weeks, confirmed by electrical conductivity measurements (detection limit = ± 0.01 µS/cm), after which the experiment was discontinued (**Figure 6B**). These findings establish that the GEM architecture can enable even hydrophilic materials to robustly entrap air upon immersion in wetting liquids. Also, a pore level scenario was presented in which the low compressibility of entrapped air and curvature of the air-water interface prevented the liquid meniscus from intruding further into the pore (**Figure 6C**).

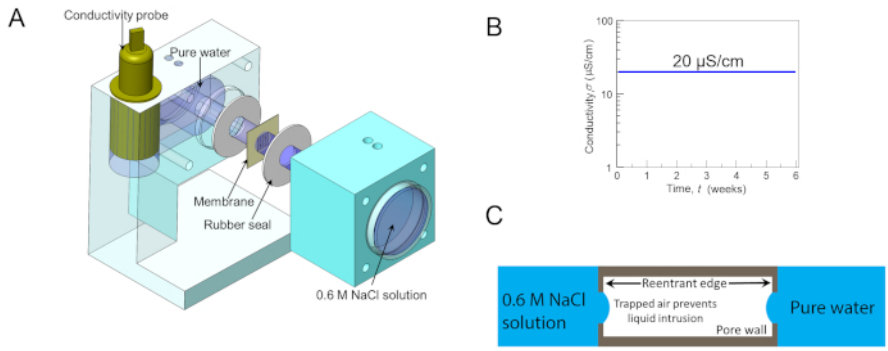

Figure 6: Membrane robustness testing. (**A**) Schematic of the 3D-printed customized cell for testing the robustness of membranes at separating dyed salty water (~0.6 M NaCl with food coloring) from pure deionized water (T = 293 K, p = 1 atm), while simultaneously logging the electrical conductivity of DI water reservoir into a computer. (**B**) A semi-logarithmic plot of the electrical conductivity of the DI water reservoir overtime when silica-GEMs were used to separate the two reservoirs. Remarkably, silica-GEMs robustly entrapped air in every pore, such that water could not penetrate even a single pore for over 6 weeks, evidenced by the electrical conductivity data. (**C**) Pore level schematic, showing the air-water interface at either end. Panels (A) and (B) are reprinted from Das et al.[37]. Please click here to view a larger version of this figure.

To gain deeper insight into movements of the air-water interface at the inlets and outlets of silica-GEMs underwater (~5 mm column), confocal microscopy was utilized. It is well-known that the laser used for illumination in confocal microscopy also heats the system[39], which can accelerate wetting transitions. Nevertheless, the high spatial resolution can yield useful insight.

For comparison, the behavior of silica surfaces with reentrant cavities was also investigated[29,40]. In both scenarios, the additional heat supplied to the water reservoir should enhance the condensation of water vapor inside the microtexture (pores or cavities). In the case of reentrant cavities, the condensation of water vapor inside the cavities displaced the entrapped air, which caused bulging of the air-water interface upwards and destabilized the system (**Figure 7A,C**). Under those experimental conditions, water intruded into all cavities in less than 2 h. In contrast, silica-GEMs remained free from bulging for a much longer period, even though the rate of heating was similar. These results were rationalized on the basis of preferential condensation of water vapor from the laser-heated reservoir on the cooler air-water interface on the other side (**Figure 7B,D**). However, it was not possible to measure the rate of mass transfer in this experimental configuration.

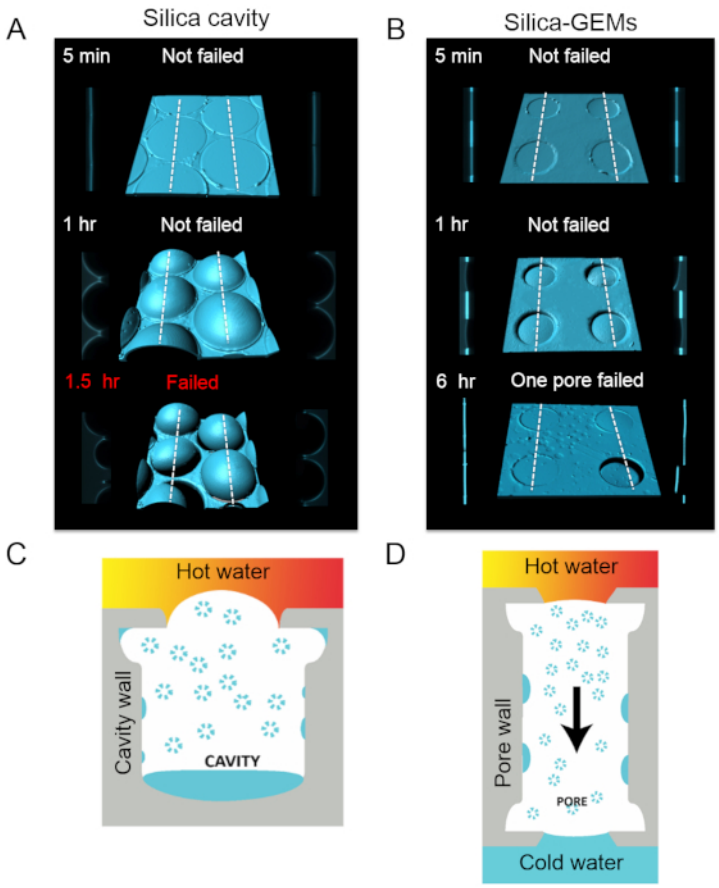

Figure 7: Air-water interfaces. (**A**) Computer-enhanced 3D reconstructions of the air-water interface at inlets of silica-GEMs underwater (column height, $z \approx 5$ mm; laser power = 0.6 mW) along with cross-sectional views along the white dotted lines (on left and right sides of the central image). Due to heating from the laser on the top side, water vapor condensed inside the cavities, displacing the entrapped air. This caused the air-water meniscus to bulge upward and become unstable. After 1.5 h, most of the cavities were intruded by water. (**B**) Confocal micrographs of silica-GEMs under similar conditions as in (A). (**C**) Schematic of the bulging of the air-water meniscus in the case of reentrant cavities underwater. (**D**) Schematic for a pore in silica-GEMs under similar conditions. Hot water vapor condenses everywhere, most notably on the cooler air-water interface on the side further from the laser. As a result of this mass transfer, there is a minimal pressure build-up in the pore. Please click here to view a larger version of this figure.

Direct contact membrane distillation with gems

Having established that Si-GEMs can robustly separate two water reservoirs on either side, a static DCMD configuration was tested, in which the salty feed side (0.6 M NaCl at $T = 333$ K) and deionized permeate side ($T = 288$ K) were static reservoirs. Even though silica-GEMs prevented water intrusion, measurable fluxes were not observed. This was due to the fact that the thermal conductivity of silicon ($k = 149$ W-m^{-1}-K^{-1})[41] is orders of magnitude higher than that of typical DCMD membranes (i.e., $k < 1$ W-m^{-1}-K^{-1})[2]. Thus, the experimental set-up with Si-GEMs suffered from what is known as temperature polarization, wherein the hot side loses heat to the cold side, lowering the flux[31].

It may be possible to reduce the thermal conductivity of silicon through nanostructuring[42] (for instance, to enhance its thermoelectric properties[43]), but these avenues were not explored. Instead, the design principles from Si-GEMs were translated to polymethylmethacrylate (PMMA) sheets ($\theta_0 \approx 70°$ for water, $k = 0.19$ W-m^{-1}-K^{-1})[40] to create PMMA-GEMs[37]. Indeed, the first (proof-of-concept) batch of PMMA-GEMs with a low porosity (of 0.08) exhibited robust separation of feed side, and it permeated and yielded a flux of 1 L-m^{-2}-h^{-1} over 90 h. Thus, it is possible to translate these Si-GEM-based studies to using more common materials for generation of greener, lower cost membranes for desalination.

Discussion

This work presents the design and fabrication of silica-GEMs, the first-ever membranes derived from hydrophilic materials that can prevent the mixing of water reservoirs on either side for over 6 weeks. Microfabrication with the SiO_2/Si system provides immense flexibility to create microtextures to test creative ideas. Of course, the scope of this work is limited to the proof-of-concept for GEMs, because SiO_2/Si/SiO_2 wafers and cleanroom microfabrication protocols are impractical for desalination membranes.

It should be noted that, even though GEM architecture can prevent the intrusion of water upon immersion when the intrinsic contact angle is (for instance) $\theta_0 \geq 40°$, this strategy fails if the surface is made superhydrophilic. For example, after exposure to oxygen, plasma silica surfaces exhibit $\theta_0 \approx 5°$, and these silica-GEMs lose air that is entrapped inside the pores spontaneously as bubbles, because the liquid meniscus is no longer pinned at the liquid-solid-air interface. However, common plastics, such as polyvinyl alcohol ($\theta_0 \approx 51$) and poly(ethylene terephthalate)

($\theta_0 \approx 72°$), should be amenable to this approach. Thus, design principles learned from Si-GEMs can be translated to realistic materials systems, such as two-photon lithography[44], additive manufacturing[45], laser micromachining[46], and CNC milling[37], etc.

Next, some crucial aspects of the microfabrication of Si-GEMs are discussed, which require special attention. The manual back alignment (section 8) of the features should be performed with as much care as possible to achieve vertically aligned pores. Offsets may result in pore-throats, and in the worst case, the misalignment may lead to only cavities on either side (no pores). Thus, it is suggested to use multi-scale alignment marks, with the smallest alignment mark being at least 4x smaller than the pore diameter.

During the etching of the silica layer with C_4F_8 and O_2 (step 10.1), prior usage (i.e., cleanliness) of the reaction chamber can influence etching rates. This is because of the presence of contaminants in the reaction chamber, a common occurrence in shared user facilities such as universities. Thus, it is recommended that this step is performed first on a dummy wafer to ensure that the system is clean and stable. Also, it is advised to use short periods for etching (e.g., no more than 5 min while monitoring the thickness of the silica layer using reflectometry). For example, if it takes 16 min to completely remove a 2 µm SiO_2 layer from a SiO_2/Si wafer, then the etching process should be divided into four steps, comprised of three 5 min cycles followed by reflectometry, and one 1 min (optional) etching step, based on the reflectometry results.

To preserve the silica reentrant features during the Bosch process that is used to etch the silicon layer (step 10.4), it is crucial that a chromium hard mask is used. The Bosch process entails the deposition of C_4F_8 to ensure the anisotropic profile. However, over long etching cycles, this layer can become very thick and difficult to remove. Thus, it is recommended that the Bosch process should not be run for more than ~200 cycles, and it should be followed by piranha cleaning. It has also been observed that long cycles of deep etching also reduce the thickness of the silica layer, despite the presence of a chromium hard mask.

Most dry etching tools fail to achieve spatial uniformity in terms of etching rates. Thus, the features obtained in the center of a SiO_2/Si wafer may not be the same as those at the boundary of the wafer. Here, high quality features were realized in the center of 4" wafers, and samples were periodically observed under a microscope. In the case that some regions are etched more than others, the wafer should be broken into pieces that should be etched separately.

This fabrication protocol can be applied to SiO_2/Si wafers of any thickness; however, a thicker layer means that a higher number of etching cycles is needed. It is suggested to use silicon wafers of <300 µm thickness, as long as this does not compromise the mechanical integrity of the wafer during handling and characterization.

Disclosures

R.D., S.A., and H.M. have filed an international patent, Application No. PCT/IB2019/054548.

Acknowledgments

H.M. acknowledges funding from King Abdullah University of Science and Technology under BAS/1/1070-01-01 and KAUST access to nanofabrication core lab facilities.

References

1. Fisher, J. B. et al. The future of evapotranspiration: Global requirements for ecosystem functioning, carbon and climate feedbacks, agricultural management, and water resources. *Water Resources Research.* **53** (4), 2618-2626, (2017).
2. Deshmukh, A. et al. Membrane distillation at the water-energy nexus: limits, opportunities, and challenges. *Energy & Environmental Science.* **11** (5), 1177-1196, (2018).
3. Ali, A., Tufa, R. A., Macedonio, F., Curcio, E., Drioli, E. Membrane technology in renewable-energy-driven desalination. *Renewable and Sustainable Energy Reviews.* **81,** 1-21, (2018).
4. Ghaffour, N. et al. Renewable energy-driven innovative energy-efficient desalination technologies. *Applied Energy.* **136,** 1155-1165, (2014).
5. Chen, J. et al. Recovery of dilute aqueous butanol by membrane vapor extraction with dodecane or mesitylene. *Journal of Membrane Science.* **528,** 103-111, (2017).
6. Wang, P., Chung, T.-S. Recent advances in membrane distillation processes: Membrane development, configuration design and application exploring. *Journal of Membrane Science.* **474,** 39-56, (2015).
7. Khayet, M. Membranes and theoretical modeling of membrane distillation: A review. *Advances in Colloid and Interface Science.* **164** (1-2), 56-88, (2011).
8. Drioli, E., Ali, A., Macedonio, F. Membrane distillation: Recent developments and perspectives. *Desalination.* **356,** 56-84, (2015).
9. Souhaimi, M. K., Matsuura, T. *Membrane Distillation. 1st edn.* Elsevier, (2011).
10. Janssen, D., De Palma, R., Verlaak, S., Heremans, P., Dehaen, W. Static solvent contact angle measurements, surface free energy and wettability determination of various self-assembled monolayers on silicon dioxide. *Thin Solid Films.* **515** (4), 1433-1438, (2006).
11. Hendren, Z. D., Brant, J., Wiesner, M. R. Surface modification of nanostructured ceramic membranes for direct contact membrane distillation. *Journal of Membrane Science.* **331** (1-2), 1-10, (2009).
12. Verho, T. et al. Mechanically Durable Superhydrophobic Surfaces. *Advanced Materials.* **23,** 673-678 (2011).
13. Boinovich, L., Emelyanenko, A. M., Pashinin, A. S. Analysis of Long-Term Durability of Superhydrophobic Properties under Continuous Contact with Water. *ACS Applied Materials & Interfaces.* **2** (6), 1754-1758, (2010).
14. Lindstrom, A. B., Strynar, M. J., Libelo, E. L. Polyfluorinated compounds: past, present, and future. *Environmental Science & Technology*. **45** (19), 7954-7961 (2011).
15. Gryta, M. Influence of polypropylene membrane surface porosity on the performance of membrane distillation process. *Journal of Membrane Science.* **287** (1), 67-78, (2007).

16. An, A. K. et al. Enhanced vapor transport in membrane distillation via functionalized carbon nanotubes anchored into electrospun nanofibres. *Scientific Reports.* **7**, (2017).
17. Hammami, M. A. et al. Engineering Hydrophobic Organosilica Nanoparticle-Doped Nanofibers for Enhanced and Fouling Resistant Membrane Distillation. *ACS Applied Materials & Interfaces.* **9** (2), 1737-1745, (2017).
18. Shi, Y. et al. A 3D Photothermal Structure toward Improved Energy Efficiency in Solar Steam Generation. *Joule.* **2** (6), 1171-1186, (2018).
19. Wang, W. et al. Simultaneous production of fresh water and electricity via multistage solar photovoltaic membrane distillation. *Nature Communications.* **10** (1), 3012, (2019).
20. Hensel, R., Neinhuis, C., Werner, C. The springtail cuticle as a blueprint for omniphobic surfaces. *Chemical Society Reviews.* **45** (2), 323-341, (2016).
21. Helbig, R., Nickerl, J., Neinhuis, C., Werner, C. Smart Skin Patterns Protect Springtails. *PLoS ONE.* **6** (9), e25105, (2011).
22. Andersen, N. M., Cheng, L. The marine insect Halobates (Heteroptera: Gerridae): biology, adaptations, distribution, and phylogeny. *Oceanography and Marine biology: an Annual Review.* **42** 119-180 (2004).
23. Cheng, L. Marine and Freshwater Skaters: Differences in Surface Fine Structures. *Nature.* **242,** 132, (1973).
24. Gao, X., Jiang, L. Water-repellent legs of water striders. *Nature.* **432** (7013), 36-36, (2004).
25. Golovin, K. B., Gose, J., Perlin, M., Ceccio, S. L., Tuteja, A. Bioinspired surfaces for turbulent drag reduction. *Philosophical Transactions of the Royal Society A - Mathematical Physical and Engineering Sciences.* **374** (2073), (2016).
26. Liu, T. Y., Kim, C. J. Turning a surface superrepellent even to completely wetting liquids. *Science.* **346** (6213), 1096-1100, (2014).
27. Domingues, E. M., Arunachalam, S., Mishra, H. Doubly Reentrant Cavities Prevent Catastrophic Wetting Transitions on Intrinsically Wetting Surfaces. *ACS Applied Materials & Interfaces.* **9** (25), 21532-21538, (2017).
28. Arunachalam, S., Das, R., Nauruzbayeva, J., Domingues, E. M., Mishra, H. Assessing omniphobicity by immersion. *Journal of Colloid and Interface Science.* **534,** 156-162, (2019).
29. Domingues, E. M., Arunachalam, S., Nauruzbayeva, J., Mishra, H. Biomimetic coating-free surfaces for long-term entrapment of air under wetting liquids. *Nature Communications.* **9** (1), 3606, (2018).
30. Hensel, R. et al. Wetting Resistance at Its Topographical Limit: The Benefit of Mushroom and Serif T Structures. *Langmuir.* **29** (4), 1100-1112, (2013).
31. Subramanian, N. et al. Evaluating the potential of superhydrophobic nanoporous alumina membranes for direct contact membrane distillation. *Journal of Colloid and Interface Science.* **533,** 723-732, (2019).
32. Wenzel, R. N. Resistance of solid surface to wetting by water. *Industrial and Engineering Chemistry.* **28** (8), 7 (1936).
33. Cassie, A. B. D., Baxter, S. Wettability of porous surfaces. *Transactions of the Faraday Society.* **40,** 0546-0550, (1944).
34. Kaufman, Y. et al. Simple-to-Apply Wetting Model to Predict Thermodynamically Stable and Metastable Contact Angles on Textured/Rough/Patterned Surfaces. *The Journal of Physical Chemistry C.* **121** (10), 5642-5656, (2017).
35. Mishra, H. et al. Time-Dependent Wetting Behavior of PDMS Surfaces with Bioinspired, Hierarchical Structures. *ACS Applied Materials & Interfaces.* **8** (12), 8168-8174, (2016).
36. Seo, D. et al. Rates of cavity filling by liquids. *Proceedings of the National Academy of Sciences.* (2018).
37. Das, R., Arunachalam, S., Ahmad, Z., Manalastas, E., Mishra, H. Bio-inspired gas-entrapping membranes (GEMs) derived from common water-wet materials for green desalination. *Journal of Membrane Science.* **588,** 117185, (2019).
38. *Manual, L.-E. U. Tanner Research, Inc.* July. (1996).
39. Xu, M. C., Sun, G. U., Kim, C. J. Infinite Lifetime of Underwater Superhydrophobic States. *Physical Review Letters.* **113** (13), (2014).
40. Seo, D. et al. Rates of cavity filling by liquids. *Proceedings of the National Academy of Sciences.* **115** (32), 8070-8075, (2018).
41. Dean, J. A. *Lange's Handbook of Chemistry.* New York; London: McGraw-Hill, Inc., (1999).
42. Yu, J. K., Mitrovic, S., Tham, D., Varghese, J., Heath, J. R. Reduction of thermal conductivity in phononic nanomesh structures. *Nature Nanotechnology.* **5** (10), 718-721, (2010).
43. Mishra, H. et al. Thermomechanical and Thermal Contact Characteristics of Bismuth Telluride Films Electrodeposited on Carbon Nanotube Arrays. *Advanced Materials.* **21** (42), 4280,(2009).
44. Liu, X. et al. 3D Printing of Bioinspired Liquid Superrepellent Structures. *Advanced Materials.* **0** (0), 1800103, (2018).
45. Jafari, R., Cloutier, C., Allahdini, A., Momen, G. Recent progress and challenges with 3D printing of patterned hydrophobic and superhydrophobic surfaces. *The International Journal of Advanced Manufacturing Technology.* 1-14 (2019).
46. Vorobyev, A., Guo, C. Multifunctional surfaces produced by femtosecond laser pulses. *Journal of Applied Physics.* **117** (3), 033103 (2015).

